Ann. Geophys., 28, 1299–1306, 2010
www.ann-geophys.net/28/1299/2010/
doi:10.5194/angeo-28-1299-2010
© Author(s) 2010. CC Attribution 3.0 License.

Annales Geophysicae

Ion-acoustic solitary waves and spectrally uniform scattering cross section enhancements

J. Ekeberg[1], **G. Wannberg**[1], **L. Eliasson**[1], **and K. Stasiewicz**[2,3]

[1]Swedish Institute of Space Physics, Kiruna, Sweden
[2]Swedish Institute of Space Physics, Uppsala, Sweden
[3]Space Research Centre, Polish Academy of Sciences, Warsaw, Poland

Received: 16 October 2008 – Revised: 15 October 2009 – Accepted: 11 June 2010 – Published: 21 June 2010

Abstract. Spectra measured by incoherent scatter radars are formed predominantly by scattering of the incident signal off ion-acoustic and Langmuir waves in the ionosphere. Occasionally, the upshifted and/or downshifted lines produced by the ion-acoustic waves are enhanced well above thermal levels and referred to as naturally enhanced ion-acoustic lines. In this paper, we study another kind of enhancement, which is spectrally uniform over the whole ion-line, i.e. the up- and downshifted shoulder and the spectral valley in between. Based on observations made with the EISCAT Svalbard radar (ESR) facility, we investigate the transient and spectrally uniform power enhancements, which can be explained by ion-acoustic solitary waves. We use a theory of nonlinear waves in a magnetized plasma to determine the properties of such waves and evaluate their effects on scattered signals measured by ESR. We suggest a new mechanism that can explain backscattered power enhancements by one order of magnitude above the thermal level and show that it is consistent with observations.

Keywords. Ionosphere (Auroral ionosphere; Plasma waves and instabilities) – Space plasma physics (Nonlinear phenomena)

1 Introduction

In incoherent scatter radar data, enhanced spectra are often seen. One such phenomenon is *naturally enhanced ion-acoustic lines* (NEIAL), which refers to spectral enhancements at the ion-acoustic frequency sometimes observed by incoherent scatter radars when the radar beam is nearly parallel to the geomagnetic field. NEIAL cover a wide range of altitudes and are interpreted as destabilized ion-acoustic waves (Rosenbluth and Rostoker, 1962). They were first seen in spectra taken by the Millstone Hill incoherent scatter radar (Foster et al., 1988) and were later also observed with the EISCAT UHF (Rietveld et al., 1991), the EISCAT VHF (Collis et al., 1991) and the EISCAT Svalbard Radar (Sedgemore-Schulthess et al., 1999; Buchert et al., 1999).

Several attempts to explain the phenomenon have been made, but so far none is completely satisfactory. A detailed review of the understanding of NEIAL during the first decade of study has been written by Sedgemore-Schulthess and St.-Maurice (2001). The generation models constitute different ways of producing the ion-acoustic fluctuations necessary for causing NEIAL. These fluctuations enhance either or both of the ion-acoustic shoulders in the incoherent radar spectra.

Based on earlier theoretical work (Rosenbluth and Rostoker, 1962; Kindel and Kennel, 1971), a current instability (= ion-electron streaming instability) has been suggested (Foster et al., 1988; Collis et al., 1991; Rietveld et al., 1991) as a mechanism for producing NEIAL observed by the Millstone Hill and EISCAT radars. Shortly after, an ion-ion two-stream instability was suggested to generate the necessary ion-acoustic fluctuations for NEIAL (Wahlund et al., 1992).

A third type of generation mechanism was suggested by Forme (1993) in the form of parametric decay of Langmuir waves. This model was later refined (Forme, 1999) to explain the altitude dependence of spectral signatures, in particular cases where both shoulders are enhanced.

Solitary waves have recently been suggested as explanations for coronal heating (e.g., Stasiewicz and Ekeberg, 2008a) and auroral acceleration (e.g., Stasiewicz and Ekeberg, 2008b). The present study investigates how

Correspondence to: J. Ekeberg
(jonas.ekeberg@irf.se)

Published by Copernicus Publications on behalf of the European Geosciences Union.

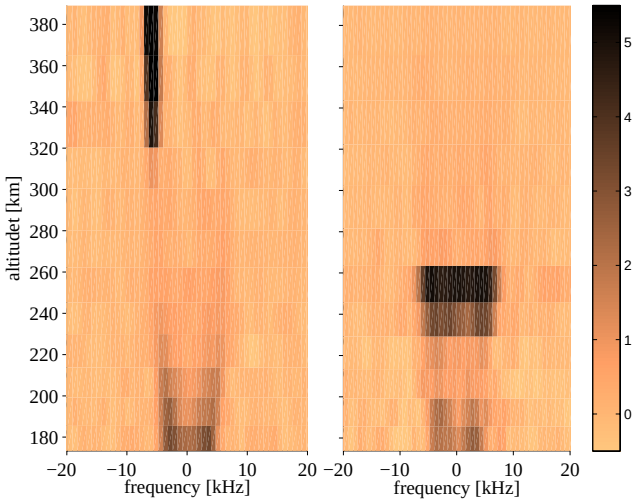

Fig. 1. Incoherent radar spectra taken with ESR. The left panel shows a typical NEIAL at altitudes above 300 km on 9 April 2007 at 11:31:54 UT. The right panel shows a different kind of spectral enhancement seen on 1 August 2007 at 00:43:00 UT. Both spectra were integrated 6 s. The colour bar shows range corrected power spectral density in arbitrary units.

ion-acoustic solitary waves could create a different type of transient enhancement of the incoherent scatter ion-line than that so far implicitly associated with the term NEIAL.

In data sets taken by the EISCAT Svalbard Radar (ESR) during the IPY (International Polar Year) operation, transient, spectrally uniform enhancements of the power in the ion-line by about one order of magnitude over a limited height range at, or close to, the F region peak have been found to be quite common. One example is shown in Fig. 1, where the left panel displays a "classical" NEIAL spectrum and the right panel shows a uniformly enhanced spectrum. The uniform type of enhancement, which leaves the ion-line spectral shape largely unchanged, is not easily explained by any of the current NEIAL models but is consistent with the model presented below.

In Sect. 2, we present ESR observations of spectrally uniform ion-line enhancements and plasma parameters used later for modelling. Section 3 introduces the model equations and discusses the characteristics of the solitary wave solutions. In Sect. 4, the suggested mechanism for spectrally uniform scattering cross section enhancements is described and results presented. The paper ends with a discussion of the model results seen in the light of the observations.

2 Observation

The EISCAT Svalbard radar (ESR) (Wannberg et al., 1997) is a 500 MHz incoherent scatter radar located on Spitsbergen at 78°09′11″ N, 16°01′44″ E. The system consists of two parabolic dish antennae of 32 m and 42 m in diameter. The former is fully steerable in azimuth and elevation, whereas the latter is fixed along the local direction of the geomagnetic field with an azimuth of 181° and an elevation of 81.6°.

Table 1. Parameter values applicable for the ionospheric F region.

Assumed values	Derived values
$N_0 = 2 \times 10^{11}\,\mathrm{m}^{-3}$	$V_\mathrm{A} = 6 \times 10^5\,\mathrm{m/s}$
$B_0 = 52\,\mu\mathrm{T}$	$\beta = 8 \times 10^{-6}$
$T_\mathrm{e} = 2000\,\mathrm{K}$	$\lambda_\mathrm{i} = 2\,\mathrm{km}$
$T_\mathrm{i} = 1000\,\mathrm{K}$	$\lambda_\mathrm{e} = 10\,\mathrm{m}$
$m_\mathrm{i} = 16\,\mathrm{u}$	
$\gamma = 5/3$	

Our example case was derived from an ESR 42 m dataset taken on 1 August 2007 with the IPY experiment. The experiment used a 32 bit alternating code (Lehtinen and Häggström, 1987) in 30 µs long pulses and had maximum range and time resolutions of 4.5 km and 6 s, respectively. It was run during one year and focused on lower heights (< 500 km), in particular the E region.

Figure 2 shows a sequence of ion-line spectra with a time resolution of 6 s and an altitude resolution of approximately 17 km, recorded between 00:42:42 UT and 00:43:30 UT. At 00:43:00 UT, the power in the ion-line at 229 and 246 km altitude suddenly peaked, reaching a level of about 4–5 times the quiescent level, after which it started to decay back to the quiescent level. The power enhancement was almost uniform across both ion-acoustic shoulders and the spectral valley, suggesting no increase of the $T_\mathrm{e}/T_\mathrm{i}$-ratio as typically seen in NEIAL-type enhancements (e.g, Forme et al., 1995). At the same time, almost no enhancement of the spectral power was seen in the height gates immediately below 229 km and above 246 km.

To get an idea of the magnitude of the enhancement, the total energy contained in the ion-line between -10 kHz and $+10$ kHz was estimated as a function of time and normalized to the level at the beginning of the event at 00:42:42 UT. This was done for each altitude bin separately. We found that at 00:43:00 UT, the ion-line power at 229 km was enhanced by a factor of four and the power at 246 km by a factor of five; six seconds later, the enhancements were down to two and four times, respectively. The duration of the strong enhancement peaking at 00:43:00 UT was at most 12 s.

The electron density profile preceding the event is shown in Fig. 3. The electron density and electron- and ion temperatures were integrated during 3 min between 00:28:48 and 00:31:48 UT and forms the parameter set, upon which the assumed model plasma in Table 1 is based. This particular interval was the last consecutive 3 min interval without abnormal spectra before the event in Fig. 2. It can be seen that the maximum spectral enhancement was taking place close to the F region peak.

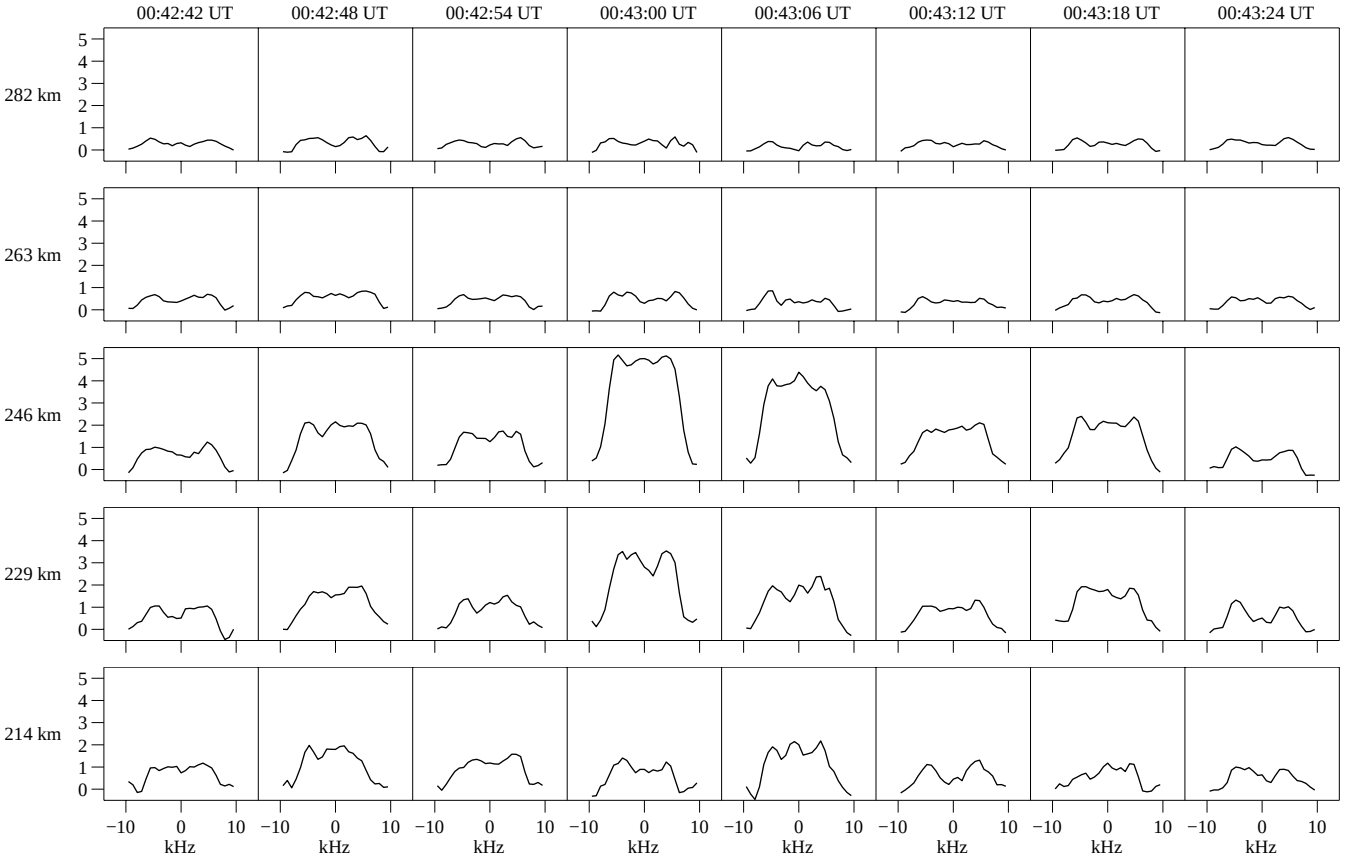

Fig. 2. Incoherent radar spectra measured with the 42 m ESR radar on 1 August 2007. The full time resolution of 6 s is used and the starting times for each integration are shown for 5 adjacent height gates, which are centered at the altitudes indicated. The x-axes show frequency and the y-axes show range corrected power spectral density in arbitrary units (common for all spectra). The spectra at 00:43:00 UT over a longer height range are shown in the right panel of Fig. 1.

3 Non-linear fluid model

We anticipate that ion-acoustic solitary structures could explain the observed spectrally uniform enhancement shown in Fig. 1. Therefore, a fluid model based on Hall-MHD with a generalized Ohm's law including electron-to-ion-mass ratio effects and electron pressure gradients, is introduced. The details are presented in the following.

3.1 Model equations

The center of mass momentum equation and the generalized Ohm's law for a collisionless plasma with singly charged positive ions and electrons are given by (e.g., Krall and Trivelpiece, 1973)

$$Nm_{\mathrm{i}}\frac{\mathrm{d}\boldsymbol{V}}{\mathrm{d}t} = \boldsymbol{J}\times\boldsymbol{B} - \nabla\cdot\mathbf{P} \tag{1}$$

$$\frac{m_{\mathrm{e}}}{Ne^2}\left[\frac{\partial \boldsymbol{J}}{\partial t} + \nabla\cdot\left(\boldsymbol{V}\boldsymbol{J} + \boldsymbol{J}\boldsymbol{V} - \boldsymbol{J}\boldsymbol{J}\frac{1}{eN}\right)\right] + \frac{1}{Ne}(\boldsymbol{J}\times\boldsymbol{B} - \nabla\cdot\mathbf{P}_{\mathrm{e}}) = \boldsymbol{E} + \boldsymbol{V}\times\boldsymbol{B}, \tag{2}$$

where $\boldsymbol{V}$, $\boldsymbol{J}$, $\mathbf{P}$ and $\mathbf{P}_{\mathrm{e}}$ are the center of mass velocity, current density, total pressure and electron pressure, respectively. In deriving Eqs. (1) and (2), collisions were neglected and $N_{\mathrm{e}} \approx N_{\mathrm{i}} \approx N$ was assumed, thus neglecting charge separation effects. The system is closed by the Maxwell's equations,

$$\nabla\times\boldsymbol{B} = \mu_0\boldsymbol{J},\ \nabla\times\boldsymbol{E} = -\frac{\partial\boldsymbol{B}}{\partial t}, \tag{3}$$

neglecting the displacement current, and two equations of state,

$$p = p_0 n^{\gamma} \tag{4}$$

$$p_{\mathrm{e}} = p_{\mathrm{e}0} n^{\gamma_{\mathrm{e}}}, \tag{5}$$

where γ and γ_{e} are the polytropic pressure exponents for total and electron pressure, respectively. The isotropic

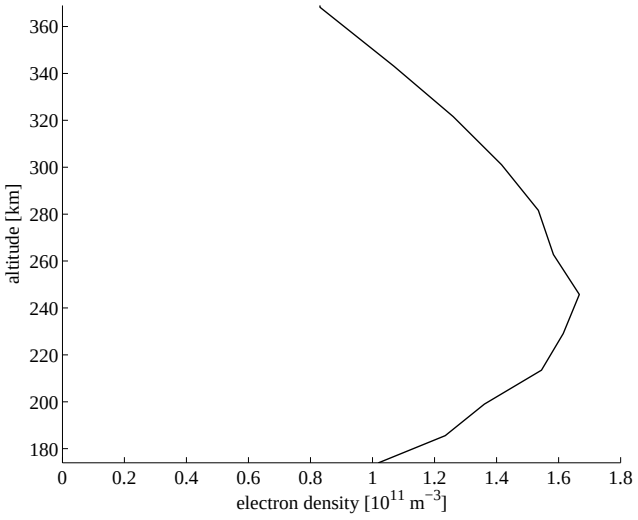

Fig. 3. Electron density profile averaged over 3 min between 00:28:48 UT and 00:31:48 UT on 1 August 2007 measured by ESR. During the interval, there was no NEIAL or other abnormal spectral enhancements.

and polytropic pressure relations are applicable for plasmas with $\beta = 2\mu_0 p_0/B_0^2 < 1$, hence for simplicity they are chosen instead of the more general polybaric pressure model (Stasiewicz, 2005b).

3.1.1 Collisions

As stated earlier, collisions were neglected in Eqs. (1) and (2). Among the collisions involving ions, neutrals and electrons, the ion-neutral collisions are expected to affect the Hall-MHD dynamics the most. The spectral enhancement in the right panel of Fig. 1 was observed around 240 km which is close to the F region peak. At these heights, the ion-neutral collision frequency is of the order of 10 rad/s (Kelley, 1989) and falls off quickly with increasing height. The linear dispersion relation of Hall-MHD shows that the growth rate associated with the wave vector used in this paper is of the order of 10^3 rad/s. Thus, the growth time of solitary structures is shorter than the collision period. Collisions are therefore expected to have a negligible effect on solitary structure formation in the present situation.

3.1.2 The wave frame of reference

In the frame of reference moving with a wave along the x-axis, NV_x' =constant (continuity equation) and B_x=constant ($\nabla \cdot \boldsymbol{B} = 0$), where the prime denotes a quantity being measured in the wave frame. Zero-indexing background quantitites and defining the magnetic field $\boldsymbol{B}_0 = B_0[\cos\alpha, 0, \sin\alpha]$, the x-component of Eq. (1) in the stationary wave frame reads

$$\frac{\partial n}{\partial x} = \left(b_y \frac{\partial b_y}{\partial x} + b_z \frac{\partial b_z}{\partial x}\right)\left(\frac{M^2}{n^2} - \frac{\beta\gamma}{2} n^{\gamma-1}\right)^{-1}, \tag{6}$$

where $M = \omega/k/V_A = -V_{x0}'/V_A$ is the Alfvén Mach number and $V_A = \sqrt{B_0^2/(\mu_0 m_i N_0)}$ for a wave travelling at speed ω/k relative to the plasma. The normalizations $n = N/N_0$ and $b_{y,z} = B_{y,z}/B_0$ have been used. According to Faraday's law, the transverse electric field in the wave frame is constant; $E_y' = -V_A B_0 M \sin\alpha$ and $E_z' = 0$. Substituting with velocity components from Eq. (1), the transverse vector components of Eq. (2) in the stationary wave frame read

$$R\frac{\partial}{\partial x}\left(n^{-1}\frac{\partial b_z}{\partial x}\right) + \frac{1}{M_\parallel}\frac{\partial b_y}{\partial x} = \left(1 - \frac{n}{M_\parallel^2}\right) b_z - \left(n - \frac{n}{M_\parallel^2}\right)\sin\alpha \tag{7}$$

$$-R\frac{\partial}{\partial x}\left(n^{-1}\frac{\partial b_y}{\partial x}\right) + \frac{1}{M_\parallel}\frac{\partial b_z}{\partial x} = -b_y\left(1 - \frac{n}{M_\parallel^2}\right), \tag{8}$$

where $R = m_e/m_i$ and $M_\parallel = M/\cos\alpha$ and x has been normalized to $\lambda_i = V_A/\omega_{ci} = \lambda_e/\sqrt{R}$, where $\lambda_{i,e}$ are the ion and electron inertial lengths, respectively. Note that $\boldsymbol{B}$ and $\boldsymbol{J}$ are uneffected by the Lorentz transformation to the wave frame in the non-relativistic case. Equations (6–8) are identical to the model used by Stasiewicz (2005a) in the isotropic case, except for a sign difference in the definition of the Alfvén Mach number, choosing here the positive sign for the propagation direction of the wave. Expressing the second-order derivatives of Eqs. (7) and (8) in terms of first order ones by letting $R = 0$, differentiating, and re-substituting gives

$$\left(1 + R - \frac{RM_\parallel^2}{n}\right)\frac{\partial b_y}{\partial x} + \frac{RM_\parallel^2}{n^2} b_y \frac{\partial n}{\partial x} = \left(M_\parallel - \frac{n}{M_\parallel}\right) b_z - \left(nM_\parallel - \frac{n}{M_\parallel}\right)\sin\alpha \tag{9}$$

$$\left(1 + R - \frac{RM_\parallel^2}{n}\right)\frac{\partial b_z}{\partial x} + \frac{RM_\parallel^2}{n^2} b_z \frac{\partial n}{\partial x} = -\left(M_\parallel - \frac{n}{M_\parallel}\right) b_y. \tag{10}$$

As seen in Table 1, singly charged oxygen ions are assumed to dominate the ionospheric F region. This justifies neglecting the electron-to-ion mass ratio R to first order.

3.2 Linearization

Linearizing Eqs. (6), (9) and (10) by perturbing the background state, $n = 1 + \delta n$, $b_y = 0 + \delta b_y$, $b_z = \sin(\alpha) + \delta b_z$, gives a system on the form

$$\dot{\boldsymbol{y}} = \mathbf{J}\boldsymbol{y}, \tag{11}$$

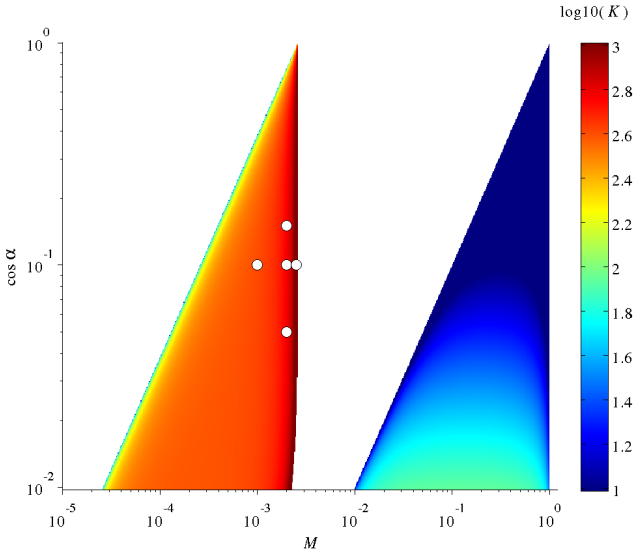

Fig. 4. Spatial growth rate K, Eq. (14), for solitary waves propagating at an angle α to $\boldsymbol{B}_0$ with the Mach number $M = \frac{\omega}{kV_A}$ in the isotropic plasma defined by Table 1. The black-edged white circles indicate the M- and cosα-values presented in Table 2, for which wave solutions are shown in Figs. 5 and 6.

where $\boldsymbol{y} = [\delta n\, \delta b_y\, \delta b_z]^T$ and $\dot{\boldsymbol{y}} = \frac{\partial \boldsymbol{y}}{\partial x}$ are column vectors and $\mathbf{J}$ is the Jacobian for the system (6), (9) and (10) evaluated at the background state. Assuming perturbations $\propto \exp(Kx)$ gives

$$\delta n = \frac{2\sin\alpha}{2M^2 - \gamma\beta}\delta b_z \tag{12}$$

$$\mathbf{M}\boldsymbol{\delta b} = \mathbf{0}, \tag{13}$$

where $\mathbf{M}$ is the polarization matrix and $\boldsymbol{\delta b} = \left[\delta b_y\, \delta b_z\right]^T$ is a column vector. Setting the determinant of $\mathbf{M}$ equal to zero gives the dispersion relation

$$K^2 = \frac{AC}{(1-RA)(1+RM_\parallel^2 C)}, \tag{14}$$

where $A = M_\parallel^2 - 1$, $C = \sin^2\alpha/\left(M^2 - \gamma\beta/2\right) - AM_\parallel^{-2}$. $R = 0$ in Eq. (14) gives the Hall-MHD dispersion relation for an isotropic plasma. K relates δb_y to δb_z through the equation

$$\delta b_y = -\frac{M_\parallel}{A}\left(RM_\parallel^2 C + 1\right) K \delta b_z. \tag{15}$$

The perturbations are fixed through Eqs. (12) and (15) by choosing δb_z. Note that especially high growth rates are expected in the vicinity of the singularity along the sonic shock line $M = \sqrt{\gamma\beta/2}$. It is seen from Eq. (14) that the two roots $K_{1,2} = \pm\sqrt{K^2}$ are either purely imaginary or real. $K^2 < 0$ corresponds to sinusoidal solutions, whereas $K^2 > 0$ describes exponentially-varying solitary waves. Based on Eq. (14), the phase diagram in Fig. 4 shows two ranges where solitary waves exist for a plasma typical in the ionospheric F region. The assumed plasma parameters are specified in Table 1. The present paper focuses on waves in the left area, just to the left of the sonic shock line ($M = \sqrt{\gamma\beta/2} \approx 3\cdot 10^{-3}$).

Table 2. M and cosα for solitary wave solutions found in Figs. 5 and 6 and indicated by black-edged white circles in Fig. 4.

M	0.001	0.002	0.0025
cosα	0.1	0.15 0.1 0.05	0.1

3.3 Wave solutions

Waves existing in the phase diagram of Fig. 4 are integrated by first assuming a density perturbation δn at $x = 0$, calculating the related transverse magnetic field perturbations δb_y and δb_z with Eqs. (12) and (15) and finally solving Eqs. (6), (9) and (10) by perturbing the background state. The perturbation is, thus, only an initial condition for the integration and the result of this perturbation will be refered to as a solitary structure. In the linear regime (white colour) of Fig. 4, a density perturbation will generate a sinusoidal density fluctuation with amplitude equal to the perturbation. The wave vector is given by the imaginary part of K.

In the solitary wave range, the wave properties are independent of the perturbation size, as long as it is small compared to the normalized background. The density perturbation δn will, however, determine the spatial growth rate of the first peak. Neither period nor amplitude of the following peaks will be affected. A change of δn by a factor 10 will displace the first peak by $\sim \lambda_e$.

In this study, a density perturbation of $\delta n = 10^{-4}$ was chosen and the corresponding transverse magnetic perturbations, for the M- and cosα-values in Table 2 (indicated by black-edged circles in Fig. 4), were calculated. The solutions with cos$\alpha = 0.1$ are found in Fig. 5, whereas the solutions with $M = 0.0025$ are shown in Fig. 6. All solutions lie within the range of solitary waves and propagate almost perpendicular to $\boldsymbol{B}_0$ with speeds slightly smaller than the ion-sound speed ($M = \sqrt{\gamma\beta/2}$). The solitary structures have full widths at half maximum (FWHM) of about 10 m.

4 Spectral enhancements induced by solitary waves

Alfvén and magnetosonic waves propagating along the geomagnetic field lines down into the ionosphere perturb the magnetic field as though compressing, twisting and plucking it. Perturbing a background plasma such as the one described in Table 1 in a manner defined by Eqs. (12) and (15) would produce solitary structures such as those in Figs. 5 and 6,

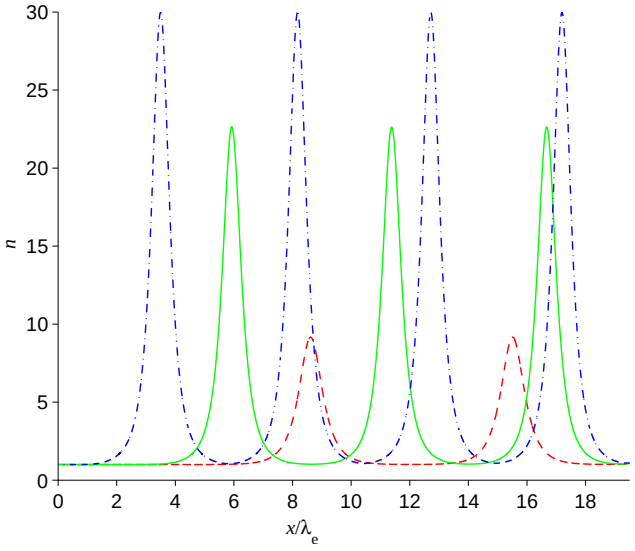

Fig. 5. The curves show normalized plasma density associated with solitary waves propagating along the x-axis at 84° angle to $\boldsymbol{B}_0$ with $M = 0.001$ (red "- -"), $M = 0.0025$ (green "–") and $M = 0.0027$ (blue "-·"). The x-axis is normalized to electron inertial length, λ_e. All structures propagate in the plasma defined by Table 1 with speeds close to the ion-sound speed ($M = \sqrt{\beta\gamma/2}$) relative to the plasma.

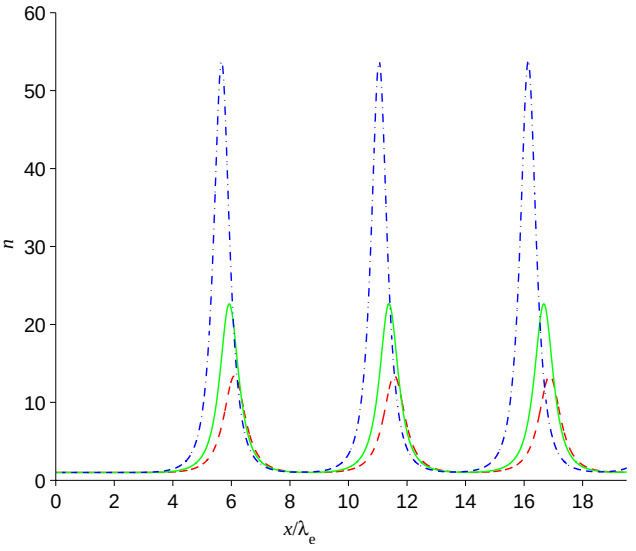

Fig. 6. The curves show normalized plasma density associated with solitary waves propagating at $M = 0.0025$ along the x-axis at 81° (red "- -"), 84°) (green "–") and 87° (blue "-·") angle to $\boldsymbol{B}_0$. The x-axis is normalized to electron inertial length, λ_e. All structures propagate in the plasma defined by Table 1 with speeds close to the ion-sound speed ($M = \sqrt{\beta\gamma/2}$) relative to the plasma.

depending on direction of propagation and speed relative to the plasma.

The geometry implied by the model equations in Sect. 3.1 for the ionosphere is illustrated by Fig. 7, where the *dip angle* θ is the angle between ground and the tangent of the geomagnetic field at a certain altitude. In the right-handed system xyz, $\hat{\boldsymbol{y}}$ points eastward and the α-angles given in Table 2 imply an $\hat{\boldsymbol{x}}$ pointing approximately to the north. Note that $\alpha = \theta$ would give a purely horizontal flow. At the location of ESR, the dip angle at 300 km altitude is approximately 80°.

Assume an isolated solitary wave propagating transversely across a radar beam oriented along the geomagnetic field. This solitary structure will supply an addition of plasma into the radar beam and thus increase the number of scatterers (electrons). Within a height gate, the radar beam can be approximated by a cylinder of height h and diameter d. Assuming a solitary structure consisting of infinitesimal slabs, each with constant plasma density N and thickness $\mathrm{d}x$, height h and width w, propagating into the radar beam, implies the geometry in Fig. 8. Since the beam cross section is circular, the transverse (to the direction of propagation) beam width w at the distance x is given by

$$w(x) = \begin{cases} 2\sqrt{x(d-x)} & , 0 \le x \le d \\ 0 & \text{else} \end{cases} \tag{16}$$

Let the beam originally be filled with background plasma of density N_0. A solitary structure with density $N(x)$ and length l in the x-direction located inside the beam would then provide the additional

$$\int_{x_0}^{x_0+l} h(N-N_0)w \,\mathrm{d}x = hN_0 \int_{x_0}^{x_0+l} (n-1)w \,\mathrm{d}x$$

number of electrons, where x_0 is the starting location of the solitary structure in the beam.

Now, assume a train of solitary structures propagating into the beam and spanning over a length equal to the radar diameter d. As the train fills the full diameter of the beam, the ratio between number of electrons in the beam with and without solitary structures is given by

$$\begin{aligned} X &= \frac{4hN_0 \int_0^d (n-1)w \,\mathrm{d}x + \pi d^2 hN_0}{\pi d^2 hN_0} \\ &= \frac{4\int_0^d (n-1)w \,\mathrm{d}x + \pi d^2}{\pi d^2}. \end{aligned} \tag{17}$$

The effective beam width of the ESR 42 m antenna is equivalent to $d = 2.5$ km at 250 km altitude. The ratio X, as defined in Eq. (17), was calculated for the structures in Figs. 5 and 6 and shown in Table 3. It shows expected scattering cross section enhancements between 3 and 10 times the quiescent level, with the highest enhancements for large M and $\alpha \approx 90°$.

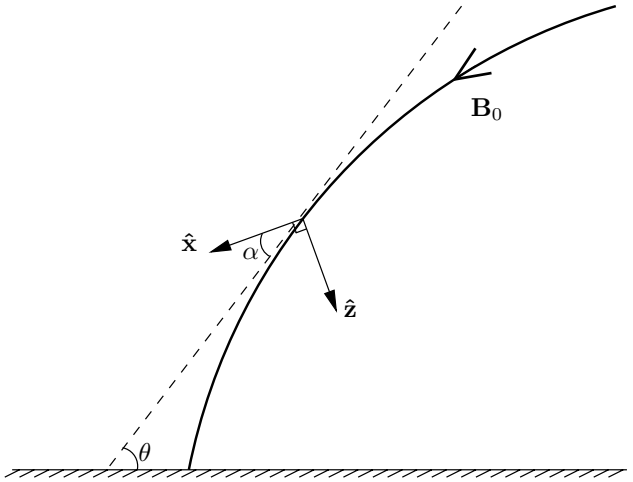

Fig. 7. Sketch of the ionospheric geometry showing the direction of propagation $\hat{\boldsymbol{x}}$ at an angle α to the geomagnetic field $\boldsymbol{B}_0$ in the xz-plane. θ, the dip angle, is the angle between ground and the geomagnetic field tangent at a certain height.

Table 3. The ratio X, defined in Eq. (17), calculated for the values of M and cosα given in Table 2 that were used to integrate the solitary waves in Figs. 5 and 6.

M	cosα	X
0.001	0.1	3
0.002	0.15	4
0.002	0.1	5
0.002	0.05	10
0.0025	0.1	7

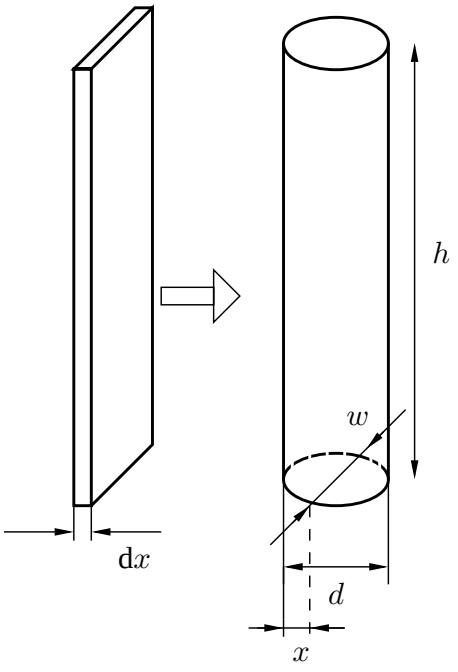

Fig. 8. A slab of infinitesimal width dx with constant plasma density propagating into a radar beam height gate of diameter d, height h and width w perpendicular to the direction of propagation.

5 Discussion

We have studied a case of spectrally uniform scattering cross section enhancement seen with ESR on 1 August 2007 between 00:43:00 UT and 00:43:12 UT. During this time, the power in the ion-line seen in the height gates centered at 229 km and 246 km altitude was enhanced by a factor of 4 and 5 times the quiescent level, at respective gates.

Plasma parameters at the observation altitude immediately before the observed event were inserted into our non-linear fluid model and ion-acoustic solitary structures were integrated, as shown in Figs. 5 and 6.

A train of such structures propagating transversely across the radar beam would carry enough additional plasma into the beam to enhance the incoherent scatter cross section to the observed level. A range of enhancements expected for different values of M and cosα, given in Table 3, are found to be in good quantitative agreement with the observations.

The relatively uniform power enhancement over the full ion-line is difficult to describe with a parametric process or any other mechanism suggested for explaining NEIAL. Also, there is no sign of T_e/T_i-ratio enhancement or asymmetry in the spectra. Since an electron beam inside or next to the beam probably would have led to a parametric process (e.g., Forme, 1993), the phenomenon is most likely initiated some distance away from the beam. We therefore assume an initiating process (such as a pumping electron beam) located several kilometres away from the radar beam. The generated solitary structure train could then gradually grow and collect plasma on its way to the beam and the density depletion, resulting from the solitary structure growth, would be spread over a long distance.

It is seen from Figs. 1, 2 and 3 that the spectral enhancement was taking place at or close to the F region peak. This is consistent with the restrictions of our model, which, due to its one-dimensionality is unlikely to be valid in the presence of strong vertical gradients. The strongly localized spectral enhancement differs essentially from observations of NEIAL, which are often seen in a height range of several 100 km at the same time (e.g, Rietveld et al., 1991).

6 Conclusions

An event of spectrally uniform ion-line enhancement was observed on 1 August 2007 by the 42 m ESR aligned with the geomagnetic field. The enhancement was at most 5 times the quiescent spectra before the event and was seen in the altitude

range 230–250 km. This altitude range includes the F region density peak. The duration of the strong enhancement was at most 12 s.

The observed spectral enhancement is different from NEIAL. The spectrally uniform enhancement over the whole ion-line is difficult to explain with any mechanism suggested for NEIAL, where either or both ion-acoustic shoulders are enhanced but in general not the spectral valley in between. Also, we do not see the T_e/T_i-ratio enhancement associated with an increased peak-to-valley-ratio often seen in NEIAL observations (e.g, Forme et al., 1995). The enhancement at study is localized to two height-gates, centered on that altitude at which vertical density gradients vanish. NEIAL, on the other hand are often observed in a height range of several 100 km.

A non-linear fluid model was used to describe solitary waves in the upper ionosphere. Perturbing the upper ionospheric plasma by shaking and twisting the magnetic field lines, compressive solitary structures were generated. They propagate transverse to the magnetic field at speeds close to the ion-acoustic speed and have perpendicular (to $\boldsymbol{B}_0$) widths of about 10 m.

A beam-filling train of the solitary waves described above would produce spectrally uniform power enhancements of about one order of magnitude above the thermal level, which is consistent with ESR observations.

Acknowledgements. J. Ekeberg thanks Thomas Leyser, Tima Sergienko and Ingemar Häggström for valuable discussions and suggestions on ground-based observations, plasma theory and EISCAT data analysis. We are grateful to two unknown referees for their valuable comments. J. Ekeberg was financed by the Swedish National Graduate School of Space Technology.

Editor-in-Chief W. Kofman thanks two anonymous referees for their help in evaluating this paper.

References

Buchert, S. C., van Eyken, A. P., Ogawa, T., and Watanabe, S.: Naturally enhanced ion-acoustic lines seen with the EISCAT svalbard radar, Adv. Space Res., 23, 1699–1704, 1999.

Collis, P. N., Häggström, I., Kaila, K., and Rietveld, M. T.: EISCAT radar observations of enhanced incoherent scatter spectra – Their relation to red aurora and field-aligned currents, Geophys. Res. Lett., 18, 1031–1034, 1991.

Forme, F. R. E.: A new interpretation of the origin of enhanced ion acoustic fluctuations in the upper ionosphere, Geophys. Res. Lett., 20, 2347–2350, 1993.

Forme, F. R. E.: Parametric decay of beam-driven Langmuir wave and enhanced ion-acoustic fluctuations in the ionosphere: a weak turbulence approach, Ann. Geophys., 17, 1172–1181, 1999, http://www.ann-geophys.net/17/1172/1999/.

Forme, F. R. E., Fontaine, D., and Wahlund, J. E.: Two different types of enhanced ion acoustic fluctuations observed in the upper ionosphere, J. Geophys. Res., 100, 14625–14636, doi:10.1029/94JA01093, 1995.

Foster, J. C., del Pozo, C., Groves, K., and St-Maurice, J. P.: Radar observations of the onset of current-driven instabilities in the topside ionosphere, Geophys. Res. Lett., 15, 160–163, 1988.

Kelley, M. C.: The Earth's Ionosphere, Academic Press, Inc., 1989.

Kindel, J. M. and Kennel, C. F.: Topside Current Instabilities, J. Geophys. Res., 76, 3055–3078, doi:10.1029/JA076i013p03055, 1971.

Krall, N. A. and Trivelpiece, A. W.: Principles of Plasma Physics, International series in pure and applied physics, McGraw-Hill Inc., 1973.

Lehtinen, M. S. and Häggström, I.: A new modulation principle for incoherent scatter measurements, Radio Sci., 22, 625–634, doi:10.1029/RS022i004p00625, 1987.

Rietveld, M. T., Collis, P. N., and St-Maurice, J. P.: Naturally enhanced ion-acoustic waves in the auroral ionosphere observed with the EISCAT 933 MHz radar, J. Geophys. Res., 96, 19291–19305, 1991.

Rosenbluth, M. N. and Rostoker, N.: Scattering of Electromagnetic Waves by a Nonequilibrium Plasma, Phys. Fluids, 5, 776–788, 1962.

Sedgemore-Schulthess, F. and St.-Maurice, J.: Naturally Enhanced Ion-Acoustic Spectra and Their Interpretation, Surv. Geophys., 22, 55–92, 2001.

Sedgemore-Schulthess, K. J. F., Lockwood, M., Trondsen, T. S., Lanchester, B. S., Rees, M. H., Lorentzen, D. A., and Moen, J.: Coherent EISCAT Svalbard Radar spectra from the dayside cusp/cleft and their implications for transient field-aligned currents, J. Geophys. Res., 104, 24613–24624, doi:10.1029/1999JA900276, 1999.

Stasiewicz, K.: Nonlinear Alfvén, magnetosonic, sound, and electron inertial waves in fluid formalism, J. Geophys. Res., 110, A03220,doi:10.1029/2004JA010852, 2005a.

Stasiewicz, K.: Ion pressure equations derived from measurements in space, Phys. Rev. Lett., 95, 015004, doi:10.1103/PhysRevLett.95.015004, 2005b.

Stasiewicz, K. and Ekeberg, J.: Electric Potentials and Energy Fluxes Available for Particle Acceleration by Alfvenons in the Solar Corona, Astrophys. J. Lett., 680, L153–L156, doi:10.1086/589878, 2008a.

Stasiewicz, K. and Ekeberg, J.: Dispersive MHD waves and alfvenons in charge non-neutral plasmas, Nonlin. Processes Geophys., 15, 681–693, doi:10.5194/npg-15-681-2008, 2008b.

Wahlund, J.-E., Forme, F. R. E., Opgenoorth, H. J., Persson, M. A. L., Mishin, E. V., and Volokitin, A. S.: Scattering of electromagnetic waves from a plasma - Enhanced ion acoustic fluctuations due to ion-ion two-stream instabilities, Geophys. Res. Lett., 19, 1919–1922, 1992.

Wannberg, G., Wolf, I., Vanhainen, L.-G., Koskenniemi, K., Röttger, J., Postila, M., Markkanen, J., Jacobsen, R., Stenberg, A., Larsen, R., Eliassen, S., Heck, S., and Huuskonen, A.: The EISCAT Svalbard radar: A case study in modern incoherent scatter radar system design, Radio Sci., 32, 2283–2308, doi:10.1029/97RS01803, 1997.